

RSC Advances



This is an *Accepted Manuscript*, which has been through the Royal Society of Chemistry peer review process and has been accepted for publication.

Accepted Manuscripts are published online shortly after acceptance, before technical editing, formatting and proof reading. Using this free service, authors can make their results available to the community, in citable form, before we publish the edited article. This *Accepted Manuscript* will be replaced by the edited, formatted and paginated article as soon as this is available.

You can find more information about *Accepted Manuscripts* in the [Information for Authors](#).

Please note that technical editing may introduce minor changes to the text and/or graphics, which may alter content. The journal's standard [Terms & Conditions](#) and the [Ethical guidelines](#) still apply. In no event shall the Royal Society of Chemistry be held responsible for any errors or omissions in this *Accepted Manuscript* or any consequences arising from the use of any information it contains.

Interface energy barrier tailoring the morphological structure evolution from ZnO nano/micro rod arrays to microcrystalline thin films by Mn doping

P. Soundarrajan and K. Sethuraman*

School of Physics, Madurai Kamaraj University, Madurai 625021, Tamil Nadu, India

Abstract

Hexagonal wurtzite crystal structure of pure and Mn doped ZnO nano/micro rod arrays (N/MRAs) thin films have been grown on ZnO nuclei layers by a cost effective chemical bath deposition (CBD). Atomic force microscopic (AFM) image clearly reiterate the growth timing of nanorods (NRs) and microrods (MRs) on seeded glass substrate under level of degree of supersaturation. The morphology of the ZnO is evolved from ZnO N/MRAs to microcrystalline structures like rods, spherulitic by interface energy barrier induced coarsening mechanism at 10% Mn doping. The preferentially oriented (0002) crystallographic plane in the undoped N/MRAs illustrate that the most of the ZnO are vertically standing on the seeded glass substrate. The stacking polar (0001) crystallographic plane in N/MRAs is suppressed by Mn doping lead to the preferential growth orientation along (10 $\bar{1}$ 0) symmetric direction at doping level 10%. The first-order high frequency E₂ mode from the hexagonal wurtzite MRs gradually experiences out-plane of unit of the coordinates with Mn doping level respectively which indicate the Mn exist in the MRs. Optical absorption and atomic crystal defects within the electronic structure of pure and Mn doped ZnO N/MRAs were then analyzed by using ultraviolet-visible (UV-vis) and photoluminescence spectroscopic technique respectively. In this work, we investigated how substrate/solution interfacial chemistry can be utilized to tailoring a new morphological structure by doping process. This interesting result will offer a new route for developing future nano/microdevices.

Key words: Chemical spray pyrolysis, ZnO nuclei layer, chemical bath deposition, crystal growth, structural and optical properties.

Corresponding author

Dr. K. Sethuraman,

E-mail: sethuraman_33@yahoo.com,

Mobile no: +919445252309.

1. Introduction

Zinc oxide (ZnO) is a direct and wide band gap (3.37 eV, 2p levels of O²⁻ valence band to 4s levels of Zn²⁺ conduction band) semiconductor and has superb and exciting properties such as large exciton binding energy (60 meV), high electron mobility and high stability at room temperature and harsh environments respectively. ZnO is one of the most popular material in the research field due to its potential use in electronic and optoelectronic devices.¹⁻⁶ Compare with another metal oxide (TiO₂, WO₃, etc.) and wide band gap materials (ZnS, CdZnS, etc.), ZnO has high phase purity, crystallinity and higher specific surface area under synthetic strategy.^{7, 8} High quality polycrystalline nature ZnO thin film has found applications in thin film transistors (TFT),⁸ light emitting diodes (LED),⁹ solar cells,¹⁰ transparent conducting electrode (TCE),¹¹ etc. While developing one-dimensional (1D) nanostructures, ZnO has attracted much attention by nanotechnologist owing to ease synthesis of ZnO produce miscellaneous nanoarchitectures such as nanorods (NRs), nanowires (NWs) and nanotubes (NTs). This provides photo excited charge carrier move freely along an axial direction owing to confine in the transverse directions. Hence it exhibits excellent structural, optical and electrical properties and is an ideal for making electronic devices.¹²⁻¹⁷ Today nano-micro scale structure is considered as an emerging high technology. The reason is that the one-dimensional (1D) nano/micro rods arrays have accelerated

research on new superstructure and utilizing them as a building block for developing nano/microelectronic devices.

Several physical and chemical deposition techniques have been employed for the preparation of ZnO nanostructured thin films.¹⁸⁻²³ Compare with physical deposition methods, the mass production cost is low in chemical methods and also it is a user-friendly. Recent days, optically transparent conducting metal oxide (TCO) thin films have been widely deposited using chemical spray pyrolysis technique,^{24, 25} it clearly reiterates the chemical spray pyrolysis can act as promising technique to deposit uniform nanoparticles films with minimum surface defects. On another hand, owing to cost effectiveness, the nanostructured thin films have been widely prepared by wet chemical methods such as chemical bath deposition and hydrothermal. Compare with hydrothermal, the precursor solution and growing films are easily discernible in CBD and also find some color changes in the mother solution during film deposition which clearly provides information about the formation of metal hydroxide, degree of supersaturation, precipitation and so on.

Rod-like, three kinds of flower-like, low and high density of NRAs, starburst, globules and micrometer sized spindle crystals have been successfully fabricated using sodium hydroxide (NaOH) and hexamethylenetetramine (HMTA) as a complexing agent on nucleation sites.²⁶⁻²⁸ Last two decades, especially in wet chemical methods, 1 D ZnO nanostructures have widely fabricated using nonionic and heterocyclic organic HMTA.²⁹ As far as the role of HMTA are not clearly identified. Recently, McPeak et al, published articles in Chem. of Mater. and Langmuir on detailed investigation of in *situ* XANES studies which suggested that the HMTA did not form a metal ion complex with Zn^{2+} in solution during ZnO nanowire growth.^{30, 31} This report clearly reveals that the role of HMTA is only for controlling the saturation index of ZnO through the

slow release of hydroxide ions. It suggested the level of degree of supersaturation in CBD growth of 1 D ZnO structure can be easily controlled using HMTA.

The nucleation process on a seed layer coated glass substrate is a pivotal point to control the characteristic dimensions of ZnO NRs. Recently, Guillemin et al. have pointed out in their work that the diameter of the NRs on seeded glass substrate should be irrespective to the diameter of the nuclei. It clearly reveals the interface energy presumably played to stimulate the underneath structural morphology of the 1 D NRs.³² For the first time, well-quality ZnO N/MRAs is directly synthesized on spray pyrolysis coated nuclei layer glass substrate through a CBD by mixed level of degree of supersaturation. It is well known that expand (or) shrinkage of interatomic spacing in 1 D nanostructure induces the changes in aspect ratio and structures. Interestingly, it has been evolved from N/MRAs to microcrystalline structures including rods, stelliform, flower and sheaf like with 3%, 7% and 10% Mn doping level respectively. After getting this unexpected morphological structure result our research group is scrutinized about interface energy. The reason is that the nucleation barrier is directly proportional to the interface energy barrier. For clear understanding the role of interface energy, the structural and optical properties of pure and 3, 7 and 10% Mn doped ZnO N/MRAs films were also desperately investigated. Our findings highlight that stimulating precisely the interface energy barrier between seed layer/bath solution under changing the level of degree of supersaturation by *in situ* doping process is essential to tailor the morphological structure of CBD ZnO N/MRAs.

2. Experimental sections

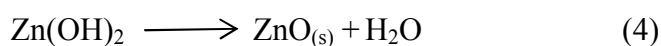
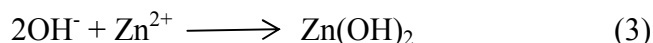
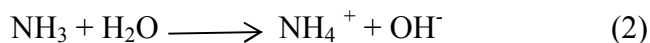
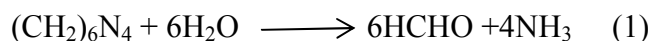
Zinc acetate dihydrate ($(\text{CH}_3\text{COO})_2\text{Zn}\cdot 2\text{H}_2\text{O}$) and manganese (II) acetate monohydrate ($(\text{CH}_3\text{COO})_2\text{Mn}\cdot \text{H}_2\text{O}$) were used as source material for Zn and Mn after purchased from Merck.

Double distilled (DD) water was used as a solvent. Hexamethylenetetramine ((CH₂)₆N₄) is also obtained from Merck. All chemicals are used in this work as received. Careful construction of coating unit is very important for easily controlling the parameters with minimum error bar. The home-built chemical spray pyrolysis and chemical bath deposition setup have been used in this present experimental work and is shown in Fig. 1(a) and (b) respectively. The noted points 1 to 7 in chemical spray pyrolysis unit are air compressor, precursor solution, nozzle, hotplate, substrate, thermocouple and exhaust and 8 to 15 in chemical bath deposition unit are thermometer, ring heater, precursor solution, magnetic stirrer, substrate holder, oil (Vanaspati), substrate and dimmerstat respectively. Commercially available cost effective microscopic glass slides were purchased from nearest scientific company. The cleaned substrate is also very important for getting uniform deposition. Therefore, microscope glass slides were carefully washed with soap solution and kept in hot chromic acid at 70 °C for 30 minutes and then subsequently cleaned in an ultrasonic bath containing double distilled water and acetone separately. The cleaned microslides were used for film coating.

0.2 M of (CH₃COO)₂Zn.2H₂O was dissolved in DD water and then stirred few minutes to obtain transparent precursor solution. The transparent aqueous solution was sprayed through a nozzle onto the preheated glass substrate at a temperature of 200 °C. The preparatory parameters were optimized and kept in constant (spray nozzle - substrate distance (25 cm), spray angle (45°), spray time (5 s), the spray interval (30 s) and compressed air (3.5 MPa)) for depositing fine nanoparticles nuclei layer. Subsequently, spray deposited thin films were annealed at 400 °C in a muffle furnace in air atmosphere for about 3 h.

The N/MRAs were grown on the spray deposited seed layer substrate using a CBD. An aqueous solution of 0.05 M (CH₃COO)₂Zn.2H₂O was taken into 250 ml conical flask and then complexes

with $(\text{CH}_2)_6\text{N}_4$ under stirring at room temperature. Nuclei layer was immersed in the metal complexed aqueous solution. The conical flask was kept in an oil bath at a temperature of $85\text{ }^\circ\text{C}$ with the help of dimmerstat connected ring heater under reflux condensation. The stepwise chemical reactions involved as follows in the final reactant CBD solution.³⁰



After 2 h deposition, the substrate was taken out from the reactant vessel, and then subsequently dried at room temperature. Similar procedure was employed for Mn doping process. However, 3, 7 and 10 mol% of $(\text{CH}_3\text{COO})_2\text{Mn}\cdot\text{H}_2\text{O}$ was added in the resultant precursor solution.

The top view surface morphology of the pure and Mn doped ZnO N/MRAs structure was analyzed by a JEOL (JSM – 5610LV) scanning electron microscope (SEM) and tilt, cross-sectional view surface morphology of the undoped ZnO N/MRAs is measured using field emission SEM (FESEM) (FEI NOVA nano SEM 600). To measuring the growth timing of ZnO N/MRAs, the 1, 1.5, 2 and 3 hour grown samples were examined by atomic force microscopy (Non-contact mode, A100 SGS, APE Research). The crystalline structure and growth direction of pure and Mn doped ZnO N/MRAs structure were determined using a Bruker D8 Advance X-ray diffraction (XRD) [$2\theta = 20\text{--}60^\circ$, $\text{CuK}\alpha = 1.54\text{ \AA}$]. The phase purity and single crystalline nature of undoped and Mn doped ZnO samples were confirmed by TEM and HRTEM (TECNAI, operated at 200 kV accelerating voltage). The X-ray photoelectron spectrum (XPS) of 7% Mn doped ZnO N/MRAs was measured using a shimadzu ESCA 3100. The optical absorption of undoped and Mn doped thin film samples were recorded in the wavelength range of 300 – 800

nm using shimadzu-UV 2450 double beam spectrophotometer. The photoluminescence spectra of the pure and Mn doped ZnO N/MRAs were analyzed using a RF-5301 spectrofluorometer in the wavelength range of 300-800 nm. The pure and Mn doped ZnO N/MRAs thin films were excited using 632.8 nm He-Ne laser line from LabRam HR800 micro-Raman instrument and recorded its backscattering mode. Thickness of the pure and Mn doped ZnO N/MRAs is measured using stylus profilometer (Mitutoyo SJ 301). Thicknesses of the pure, 3, 7 and 10% Mn doped ZnO N/MRAs are 5 ± 0.5 and $4 \mu\text{m}$ respectively. Further, the thickness of the pure ZnO N/MRAs is also verified with the cross-section SEM image (Fig. S1(b)).

3. Results and discussion

Fig. 2(a) shows the low and high magnification SEM image of ZnO N/MRAs thin film. The ZnO NRs are vertically and beautifully standing on the seed layer coated glass substrate indicates the footprint of the seed layer containing high density and homogeneously textured (crystallinity) polar c-plane nuclei. The sprout of NRs on polycrystalline nanodots is owing to the energetic surface of specific crystallographic planes (or) facets can easily find the place for sitting (or) bedding under epitaxial relation between reactant solution and seeded substrate with respect to lattice mismatch. Then they stimulate crystal growth along an axial lattice parameter direction. The length and diameter of the ZnO NRs are 500 ± 50 nm and 150 ± 20 nm is measured using 3 D AFM (Fig. 3(b)) and high magnification SEM (Fig. 1 (a)) image respectively. The ZnO MRs has grown atop ZnO NRs and its alignment parallel to the substrate with random distribution overall the NRs. In general, it is well known that the large scale synthesis of nano/micro structure is very important for fabricating nano/microelectronic devices. The diameter and length of the ZnO MRs are $2 \pm 0.5 \mu\text{m}$ and $6 \pm 0.5 \mu\text{m}$ respectively indicate that the solution based routes are

very facile and promising method to produce N/MRAs and this is difficult to fabricate by physical methods including sputtering and chemical vapor deposition (VS and VLS transformation). Both ZnO NRs and MRs have a hexagonal shape in structure due to the alternately stacked hexagonal shaped crystallographic facets growth of tetrahedrally coordinated Zn^{2+} and O^{2-} ions owing to fast growth of energetically favorable basal surface. More importantly, another ZnO N/MRAs have been grown by using same experimental condition for checking reproducibility. Fig. 2(b, c and d) shows the surface morphology of the 3, 7, and 10 % Mn doped ZnO nano/micro scale structure thin films. When the doping percentage is three, the diameter of the NRs decreased and number of MRs increased with changes in the aspect ratio and size. Further, increasing Mn doping concentration to 7%, the diameter of NRs is shrinking twice (50 ± 20 nm) as compared to the undoped N/MRAs (150 ± 20 nm) and as well as the diameter of the MRs is slightly increased with small changes in aspect ratio. Hence, the average density of the NRs is increased with Mn doping up to 7%. The average density of the NRs for pure ZnO N/MRAs is ~ 37 NRs/ μm^2 and increased $\sim 54, 73$ NRs/ μm^2 with respect to 3 and 7% Mn doping level respectively. Finally, increasing Mn doping concentration to 10%, the ZnO NRs do not grow on the seed layer coated glass substrate. Interestingly, here it is observed that the randomly distributed exotic MRs and microcrystalline sheaf and spherulitic morphology overall the seeded substrate. From this result, it is realized that the interface energy presumably played an important role during the initial growth of films. Hence, we plausible that this result is caused by interface energy hold in hand to control the level of degree of supersaturation and this will be clearly discussed in the forthcoming part.

In order to understand the growth mechanism of NRs and MRs on seed layer coated glass substrate, we have systematically prepared a serious of samples with respect to different growth

time (1, 1.5, 2 and 3 h). The AFM images for 1.5, 2 and 3 h grown samples were not able to measure at different spot area, which presumably reiterate that the up to 1 h the MRs did not grow on there. Fig. 3 (a, b) shows the 2D and 3D AFM image of ZnO NRs grown on seeded glass substrate at growth time of 1 h. Thickness of the NRs is 0.5 μm . It is well known that the growth of NRs on a rough or seeded substrate using chemical route is only by heterogeneous nucleation. Collaborate each result is very important for determining the quality of the work under identical conditions. Therefore, the top of the hexagonal shaped NRs from 2 D AFM image clearly checked with the top view of high-magnification SEM image. When increasing growth time above an hour, we could not take AFM image at different spot area of the prepared samples. The reason is that the ZnO MRs started to grow randomly on NRs covered substrate after an hour. Govender et al. observed this kind of homogeneous precipitates oriented attachment due to difficulty to distinguish the template layer at shorter growth time. It was found that the degree of supersaturation high at the initial stage of the chemical reaction due to the high concentration of ions which induces to form a homogeneous precipitations.^[33] But, hitherto, the formation of MRs is unclear. In general, the degree of supersaturation is divided into three types (i) low, (ii) intermediate and (iii) high. The predominance of one over other determines the velocity of growth in a particular direction from the solution. The careful watching of solution during film growth clearly reiterates the following points under level of the degree of supersaturation. The low degree of supersaturation stimulates the heterogeneous nucleation on seed layer of polycrystalline ZnO crystallites owing to lower growth rate. Further, it induces to form an edged hexagonal faces and thermodynamically stable prismatic ZnO NRs which subsequently elongate parallel to the c-axis. The polynuclear processes is occur at intermediate degree of supersaturation, therefore 2 D growth predominates by the mixture of

slow spiral growth. In our experimental work, owing to intermediate degree of supersaturation, the horizontally aligned monodispersed ZnO microrod crystals are promoted on the vertically standing NRs after an hour as the color of the solution changed. The solubility product between Mn and Zn is different and hence it stimulates different degree of supersaturation in the precursor solution with respect to growth time and percentage of impurity ion doping. We found that the interface energy plays a crucial role for determining the degree of supersaturation in the mother solution. The decrease in the diameter of the ZnO NRs with Mn doping might be resulted from the degree of supersaturation try to change into the intermediate from low by interface energy tension.

Hence, in CBD process, the most rapid growth rate of crystallographic facet (0001) of ZnO easily found the nucleation sites on the high density nuclei nanoparticles and build the bottom basal plane at low degree of supersaturation with respect to crystalline size of the nuclei and space distance between neighboring nuclei particles. At 10% Mn doping, the supersaturation is intermediate and high. Therefore, the MRs is randomly distributed on the seeded substrate in the intermediate degree of supersaturation solution environment. In some places, the MRs are try to build different microstructures including stelliform and flower-like owing to oriented attachment of homogeneous precipitates owing to high degree of supersaturation. The flower-like rod bunches is composed of closely packed submicrometer- sized rods with diameter of 400-600 nm and lengths of 2-3 μm . The stelliform structures are composed of one long rod standing erectly with length and diameter of 4 μm and 300 nm, and as well as several microrods are radially growing at the bottom of the erectly rod. In general, the hexagonal shaped (0001) crystallographic facets are containing Zn atomic layer environment with most stable surface. The reason is growth rate of hexagonal ZnO crystal structure follows the sequence (0001) > ($\bar{1}01\bar{1}$) >

$(\bar{1}010) > (\bar{1}011) > (000\bar{1})$. From our observed result, the most rapid growth rate grown polar basal plane (0001) of top of the NRs and bottom and top of the MRs indicate that the growth rate not rapidly increased with Mn doping. It is only playing with the interface energy between crystal nuclei and seeded substrate with the help of degree of supersaturation. Therefore it evaluates the surface morphologies from 1 D nano/micro meter scale to micro. Panigraphy et al. have fabricated Mn-doped ZnO NRs via a simple one-step aqueous –based chemical method and the size of the NRs was increased with Mn doping as compared with the pure ZnO.³⁴ Recently, the same behavior was also observed by the Singh et al.³⁵ The shrinkage of diameter of NRs under increasing Mn doping percentage is also promote to increase the air gap between NRs. This indicates the higher surface energy of ZnO crystallographic plane ions (negatively charged O planes and/or positively charged Zn planes) from the reactant solution find the center point in the nuclei nanoparticles and initiated to start growth from there. We conclude that the diameter of the NRs shrinkage from their middle point of the nuclei particle with respect to interface energy barrier. It is also reported the diameter of the ZnO nanoarrays increased with increasing precursor concentration.³⁶ Recently, 11% efficient perovskite solar cell based on ZnO NRs optimized by controlling the diameter of the NRs.^[37] Furthermore, it is interesting to see that the nucleation force from the seed substrate fully stopped at 10% Mn doping. After getting this morphological result our research team takes an account to deeply thinking about the interface energy. The reason may be due to degree of supersaturation changed from low, intermediate to intermediate, high by barrier of interface energy. Fast crystal growth at high supersaturation degree induced the formation of spherulitic structures mostly over the MRs by interface energy tension. It is found that the homogeneous and heterogeneous nucleation on seed layer covered substrate under changing level of degree of supersaturation by doping process in CBD.

Pure N/MRAs, 7 and 10 % Mn doped ZnO N/MRAs were subjected to TEM characterization and is shown in Fig. 4(i, iv), 5(i, iv) and 6(i-iv) respectively. The formation of NRs, MRs from pure, 7% Mn doped ZnO N/MRAs and flower, star, sheaf and stelliform-like structures from the 10% Mn doped ZnO N/MRAs is authentically confirmed by TEM characterization. Growth orientation and single crystalline nature and hexagonal wurtzite crystal phase of the pure and Mn doped films is also confirmed by HRTEM and SAED patterns. Generally, ZnO has three types of crystallographic facets, a polar $\{0001\}$ facet and two nonpolar $\{2\bar{1}\bar{1}0\}$ and $\{01\bar{1}0\}$ facets. As shown in the HRTEM images from Fig. 4(ii, v) and 5(ii, v), the facets of the NRs and MRs of pure and 7% Mn doped ZnO N/MRAs is $\{0001\}$ and $\{01\bar{1}0\}$ respectively and checked with the corresponding SAED pattern from Fig. 4(iii, vi) and 5(iii, vi). Both are perpendicular to the (0002) crystallographic planes. HRTEM and SAED pattern have taken from flower like structure on 10% Mn doped ZnO film which suggests they grow along the $\{0001\}$ facet and shown in Fig. 6(v, vi). Our observed result is well collaborated with the reported value.^{38,28}

From XRD analyses, the ZnO nanostructures show a predominant $(10\bar{1}0)$ Bragg reflection peak at 2θ value 31.44° representing a preferential growth along a- or m- axis parallel to the substrate.³⁴ It was also noticed that the ZnO nanostructures consist Bragg reflection at 2θ value 34.44° due to (0002) crystallographic plane implies that most of the nanostructure are aligned vertically along the c-axis.³⁹ The ZnO nanosheet exhibits predominant Bragg reflection at 36.10° corresponding to the $(10\bar{1}1)$ symmetric reflection.⁴⁰ These results reiterate that the morphological structure of the hexagonal wurtzite ZnO mainly depends on the following Bragg reflections such as $(10\bar{1}0)$, (0002) and $(10\bar{1}1)$. The predominant diffraction peak intensity in the order of $(10\bar{1}1) > (10\bar{1}0) > (0002)$ exhibits the nanoplate morphology prepared by CBD.³⁸ Further, the flower

like morphology observed on soda-lime glass slide due to the crystallographic plane growth in the order of $(10\bar{1}1) > (10\bar{1}0) > (0002)$ and $(0002) > (10\bar{1}0) > (10\bar{1}1)$.⁴¹ Xu et al have investigated stelliform like morphology on Au/glass substrate and this result clearly revealed that the crystallographic plane growth order is $(10\bar{1}1) > (0002) > (10\bar{1}0)$ stimulating stelliform-like morphology.⁴²

Fig. 7 shows the X-ray diffraction patterns of the pure and 3, 7 and 10 % Mn doped ZnO N/MRAs thin films. The XRD pattern of the ZnO N/MRAs consisting of diffraction peak at 2θ values 31.80° , 34.48° , 36.29° , 47.52° , 56.62° , 63.02° , 62.97° , 66.42° , 67.97° and 72.57° corresponding to the coordination Bragg reflections $(10\bar{1}0)$, (0002) , $(10\bar{1}1)$, $(10\bar{1}2)$, $(11\bar{2}0)$, $(10\bar{1}3)$, $(20\bar{2}0)$, $(11\bar{2}0)$, $(11\bar{2}2)$ and $(20\bar{2}1)$ respectively. This is well matched with the JCPDS card no (36-1451) and previously reported works. Bragg reflections corresponding to polar c-plane and non-polar m, a-planes in XRD is clearly reveals the strong orientation along a specific direction. The hexagonal wurtzite structure with edge of the m-planes indicates the anisotropic growth tendency of ZnO NRs. The second preferentially oriented Bragg reflection $(10\bar{1}0)$ implies that the some of the ZnO 1D structure are growing along a-axis. Furthermore, it is concluded that the order of the Bragg reflection $(0002) > (10\bar{1}0) > (10\bar{1}1)$ is stimulating the ZnO N/MRAs on seed layer coated glass substrate. As compared to pure ZnO N/MRAs, the intensity of the $(10\bar{1}0)$ and (0002) coordination symmetric reflections increased in 3% Mn doped ZnO N/MRAs. It may be due to the increase in the number density and/or stimulate existing growth orientation of the N/MRAs. This result is well collaborate with the SEM image where the number of NRs increased with respect to decreasing NRs diameter and number of MRs increased with respect to changing aspect ratio as shown in the inset of XRD. It has been stated that the particular percentage of impurity doping such as Ag and Co in ZnO NRs, the intensity of the

(10 $\bar{1}$ 0) crystallographic plane was increased.⁴³ The 10% Mn doping in N/MRAs, the predominant peak changed to (10 $\bar{1}$ 0) Bragg reflection is observed, which ratify the most of the ZnO crystallographic plane grow along a-axis. The order of Bragg reflection in 10% Mn doped ZnO N/MRAs is (0002) < (10 $\bar{1}$ 1) < (10 $\bar{1}$ 0) and induces the microrods, stelliform and flower like structure on seeded substrate under interface energy barrier induced coarsening mechanism. The major (10 $\bar{1}$ 0), (0002) and (10 $\bar{1}$ 1) Bragg reflections slightly shifted due to out-plane of lattice parameter of the host ZnO lattice by doping. In the end, we conclude that the highest (10 $\bar{1}$ 0) Bragg reflection is obtained at 10% Mn doped ZnO clearly reveal that the Mn ions in the ZnO MRs structure enhance the growth rate along the (10 $\bar{1}$ 0) crystallographic direction.

Fig. 8(a-c) shows the Zn 2p, O 1s and Mn 2p XPS spectra recorded in the 7% Mn doped ZnO N/MRAs film. Two strong peaks centered at 1025.5 and 1049.0 eV attributed to the binding energy of Zn 2p_{3/2} and Zn 2p_{1/2} respectively, and is shown in the Fig. 8(a). Each Zn ion is in the +2 valence state is confirmed by the 23.1 eV of spin-orbital splitting. Fig. 8(b) shows the O 1s XPS spectrum. Lorentz fitting of the O 1s peak gives two peaks centered at 533.78 and 535.04 eV attributed to the O-Zn binding energy in the hexagonal ZnO lattice and O²⁻ ions in the oxygen deficient region within the host lattice. To identify the dopant in the host crystal lattice, we displayed 638 to 660 eV range and is shown in Fig. 8(c). The Mn 2p_{3/2} and Mn 2p_{1/2} state confirmed by the two strong peak at 642 and 656 eV and gives the clear evidence for the presence of Mn in the hexagonal ZnO N/MRAs. The spin-orbit interaction of Mn 2p_{3/2} and 2p_{1/2} peaks are appear that indicate the Mn with value of Mn⁴⁺ and Mn³⁺ oxidation state.

The recorded UV-vis absorption spectra are shown in the Fig. 9(a) in the energy range of 1.55-3.82 eV. The ZnO N/MRAs allowed absorption around 400 nm and this is characteristic absorption of ZnO structure. For clear understanding of changes in electronic state of ZnO

N/MRAs, UV-vis absorption spectra were taken for the Mn doped ZnO N/MRAs. Recently, we have investigated the light trapping effect on 1 D TiO₂ NRs depends on the number density and large size.⁴⁴ For clear identification of absorption edge, the enlarged view of spectra is shown in the inset of absorbance spectra. The absorption edge blue shifted with increasing doping concentration indicate the enlargement of energy band gap of ZnO N/MRAs with Mn doping concentration. This is well consistent with the reported value.³⁵ The forbidden band width was calculated using Tauc's method and is shown in the Fig. S2.

The photoluminescence analysis is one of the most important tools to analyze the material quality. Because, the doping induced impurity atomic defect states such as oxygen vacancies (V_o), zinc vacancy (V_{zn}), interstitial Zn (Zn_i), interstitial O (O_i), Zn antisite (Zn_o) and oxygen antisite defects O_{zn} (oxygen at zinc site) within the host material electronic structure is extensively investigated by photoluminescence spectrum. When exist the above-mentioned defect states in the wide band gap ZnO structures, the charge carriers are relaxed at particular impurity state within the electronic states. Therefore, it stimulates corresponding defects level emission in the visible regions. It is well known that the prepared material quality is confirmed by intensity and/or width of the near band edge emission (NBE) which arose due to the recombination of free excitons such as electron and hole pair (band to band transition O_{2p} to Zn_{3d}) through an exciton-exciton collision process. Hence, we have carefully subjected our pure and Mn doped ZnO N/MRAs samples to PL analysis with excitation wavelength of 325 nm. The representative recorded PL spectra for pure and Mn doped ZnO N/MRAs are shown in the Fig. 9(b).

The defect states of the 1 D ZnO nano/micro structure strongly depends on their crystalline and morphological structures. The PL spectrum of pure ZnO N/MRAs exhibits the

combine UV, broad violet (380- 420nm), blue (450 and 470 nm) and green (560 nm) emissions. The existence of impurity state within the material electronic state exhibits the visible emissions indicates the presence of point defects in the ZnO N/MRAs. Nevertheless, the violet and blue transition corresponding to the point defects such as V_{zn} and Zn_i . The impurity states called as donor (or) acceptor with respect to which place it is positioned from the valence band maxima and conduction band minima. Hence, the Zn_i , V_o and V_{zn} , singly ionized zinc vacancy (V_{zn^-}) are known as shallow level donor and acceptor respectively. However, despite high crystalline nature of prepared samples observed from XRD, the NBE is combining with violet emission and seems to be broad and not well resolved. This is may be due to point defect from the seed layer such as Zn vacancies. The NBE (electronic state of host material) of 10% Mn doped ZnO N/MRAs is slightly blue shifted as compared to pure ZnO N/MRAs, indicate the slightly expansion of material electronic state and it is well matched with the UV-vis absorption spectra. We assume that the broad violet emission centered around 410 nm due to the charge carrier transition from the conduction band minima to the acceptor V_{zn} level and this transition confirm the presence of Zn vacancies in the electronic state of ZnO N/MRAs. Further, the singly ionized Zn vacancy (V_{zn^-}) state stimulate blue emission due to the charge carriers have relaxed at this particular impurity state. A broad emission peak around 560 nm attributed to V_o and this green emission corresponding to the charge carrier transition from V_o to V_{zn} . Furthermore, the blue and green emissions confirm the existence of the oxygen and zinc vacancies in the undoped and Mn doped ZnO N/MRAs. From the SEM images, the diameter of the NRs decreased by Mn doping under interface energy barrier induced zinc vacancies and increased air gap between NRs. This is reason for V_{zn^-} , V_{zn} and V_o impurity states are increased up to 7% Mn doping. In the case of 10%

doping, the V_o decreased owing to disappear of NRs not allowed air gap which also discount the light trapping effect. Hence, here only the V_{zn} is increased.

Our as-prepared pure and Mn doped ZnO N/MRAs examined to μ -Raman scattering at room temperature. Wurtzite ZnO crystal structure belongs to the $C46v$ ($P6_{3mc}$) symmetry group with 4 atoms (two formula units) per primitive cell. According to group theory, ZnO has nine optical and three acoustical phonon (Brillouin scattering) branches for a given phonon wave vector. The optical phonon mode at near the center of the Brillouin zone can be expressed.⁴⁵

$$\Gamma_{opt} = A_1 + 2B_1 + E_1 + 2E_2$$

In ZnO, the coulomb field due to the bond (both ionic and covalent) between atoms leads to the splitting of the A_1 and E_1 modes into longitudinal optical (LO) and transverse optical (TO) phonon. The $2B_1$ symmetry phonon modes are both Raman and IR active. The $2E_2$ modes are non-polar and Raman active. The atoms experience movement parallel and perpendicular to the c-axis with respect to A_1 and E_1 modes respectively. The A_1 and B_1 modes exhibit atomic displacements along c-axis, whereas the E_1 and E_2 give atomic displacements perpendicular to the c-axis. Therefore, the mechanical strength of the material strongly depends on the vibrational modes. The low frequency E_2 mode is associated with the lattice vibration of Zn atoms, and the high frequency E_2 mode is attributed to the vibration of the oxygen atoms from the hexagonal wurtzite crystal structure. The displayed Raman bands in Fig. 10(a) is recorded from the visible microrods in the pure, 3, 7 and 10 % Mn doped ZnO N/MRs through corresponding optical image as shown in Fig. 10(b).

From Fig. 10(a), the narrow full width at half maximum with sharp and predominant Raman peak at 98 cm^{-1} is attributed to the nonpolar optical phonon modes of ZnO corresponding to low-frequency E_2 mode, which associated with the lattice vibration of Zn atoms from the sub-lattices

of ZnO. A weak broad band shows at 332 cm^{-1} corresponding to the second-order phonon of the low-frequency E_2 . In the inset of pure ZnO N/MRAs Raman spectrum, the top view of the schematic hexagonal wurtzite structure system denoted from the high frequency E_2 mode, which also indicate the formation of hexagonal wurtzite structure. Further, the strain, composition and phase orientation of hexagonal ZnO structure are also described by the first-order high-frequency E_2 mode. The corresponding phonon mode shows at 437.8 cm^{-1} for pure ZnO N/MRAs and 437.2 , 436.9 and 436.2 cm^{-1} corresponding to 3, 7 and 10% Mn doped ZnO N/MRAs films respectively. The high-frequency E_2 Raman peak of the Mn doped ZnO N/MRAs was red shifted as compared to the pure ZnO N/MRAs which indicates that the local stress arising as a result of a change in the N/MRAs morphology with incorporation of Mn^{2+} ions into the Zn^{2+} lattice sites.

When fabricating ZnO NRs, the shaft and cap of the NRs can be easily changed by preparatory parameters. It was noticed that the amount of Mn in ZnO NRs were much lower than the amount added as Mn source in the precursor of the chemical bath.³⁸ The reason is higher bond energy for Mn-O compared to Zn-O requires more energy to replace Zn^{2+} by Mn^{2+} in ZnO lattice. In our case, as compare to pure ZnO N/MRAs the horizontally aligned MRs aspect ratio changed and number density increased with Mn doping level respectively indicates that the Mn^{2+} ions successfully enter into tetrahedral coordinated Zn^{2+} sites of MRs. It was also explained that the higher bond energy of Mn-O could assist the coalescence process in Mn doped ZnO NRs and then they allow to increases the diameter of the NRs.⁴⁷

Compare with previous report, here for the first time diameter of the NRs decreased up to 7% Mn doping level. It is also noticing that the aspect ratio and diameter of the MRs are slightly changed. After searching reason for this, we found one point that the solubility of Mn^{2+} ions in ZnO lattice is $\sim 14\%$.⁴⁸ Hence, the incorporation of Mn^{2+} ions in ZnO lattice site via a low

temperature method is still conundrum. When we introduced Mn^{2+} ions during initial growth of ZnO NRs under lower growth rate, the lattice mismatch between the growing crystal plane and nanoparticle nuclei substrate is disturbed. Moreover, the host material crystal nuclei competitive with foreign impurity and try to balance the lattice mismatch. In this crystal growth environment, the host crystal atoms find the suitable sitting place on the seed substrate after fighting with foreign impurity atoms. Hence, the 1 D NRs diameter of growing host material is gradually confined up to 7% Mn doping, which induces to continuously decrease the diameter of the NRs. Hence, the degree of supersaturation is also changed by the interface energy. The NRs did not grown at 10% Mn doping and here only MRs emerged on seed layer coated glass substrate indicates the interface energy barrier is not allowed the low degree of supersaturation in the reactant solution.

In order to understand the influence of interface energy we have deeply investigated μ -Raman scattering. Because of, μ -Raman is very sensitive tool to record the spectrum within 1 μm spot area of the sample. The spot area is selected by the optical image. The ZnO MRs is clearly visible through optical image and visible darkness area of the sample is realized to known as presence of NRs and space between each NR (air gap). We have taken μ -Raman spectra from different spot area of darkness place of pure, 3% and 7% Mn doped ZnO N/MRAs thin films. Particularly, two dominant Raman band such as E_2 low and E_2 high mode is observed from the NRs. Here the E_2 high Raman mode does not shifted in wavenumber region and this clearly indicates the Mn^{2+} ions do not located in the NRs. If impurity entered into the NRs, it surely experiences the compressive strain.⁴⁹ Thereafter, Raman spectra have recorded from the MRs. Here the E_2 high mode is slightly shifted towards lower wavenumber region and is shown in the Fig. S3(a). This Raman band shift authentically revealed that the Mn^{2+} ions only enter in the ZnO

MRs. Here, during crystal growth, the low supersaturation does not allow to enter dopant ions into host material crystal lattice of NRs. Therefore, when increasing doping concentration, the number of MRs increased with changes in aspect ratio and diameter. From the XRD, we concluded that the reorientation of crystallites (0002 to 10 $\bar{1}$ 0) occur at 10% Mn doped ZnO N/MRAs indicate the vertically standing c-plane NRs crystal growth is totally changed along m-plane direction by experiencing compressive strain and is shown in Fig. S3(b). The reason is when increasing the dopant concentration, the higher competition between two (host and impurity) releasing of metallic ions from the complex does not allow for finding the nucleation sites vice versa on the seeded substrate. During finding, the sufficient amount of cation ions immediately produced in the reactant solution that favors to change the degree of supersaturation from low to intermediate. As a consequence, the nuclei layer has disappointed to balancing the interatomic spacing value in this chemical solution environment, which facilitate the formation of interface energy barrier. Hence, the horizontally aligned ZnO MRs promote along a-axis when the reorientation crystallites occur. It clearly reiterate the when engineering the crystal at low supersaturation degree, the foreign impurity atoms not entered to building the crystal growth owing to carefully finding the host crystal planes from the solution under lower growth rate. Here we have fabricated exotic and new surface morphology under degree of supersaturation with respect to Mn doping and their growth behavior is shown in Fig. 11. This kind of result obtained for the first time in Mn doped ZnO N/MRAs thin films and this interesting nano/micro and micro meter size structured ZnO thin films can be envisaged as potential candidates for developing future nano/microelectronic devices.

4. Conclusions

In this work, the interface energy barrier between nuclei NPs and NRs by Mn doping is first highlighted by us. First, well-quality ZnO N/MRAs successfully fabricated by well-known low cost chemical deposition method under mixed degree of supersaturation. The growth timing of NRs and MRs has analyzed by AFM. The effect of metallic Mn ions on ZnO N/MRAs is systematically investigated by TEM, XRD, XPS, UV-vis, photoluminescence and micro-Raman spectroscopy. With respect to 3 and 7% Mn doping, the diameter of the NRs decrease and aspect ratio of MRs changed with increasing. At 10% Mn doping, m-plane MRs, spherulitic and sheaf structures are arose on seeded substrate. Further, the obtained structures are authentically confirmed by TEM characterization. Hexagonal wurtzite structure of pure and Mn doped ZnO N/MRAs is confirmed by XRD and μ -Raman scattering. It is also noticed the changes in the surface morphology from NRs to microcrystalline structure at 10% Mn doping stimulate the reorientation of crystallites from c- to a-axis. From μ -Raman scattering, it is confirming the Mn^{2+} ions only enter into the MRs by E_2 high mode corresponding to hexagonal wurtzite structure experience a compressive strain. The absorbance, absorption edge and energy band gap values with Mn doping on ZnO N/MRAs were analyzed by UV-vis absorption spectra. The presence of impurity state within the host ZnO N/MRAs by Mn doping is characterized by the PL spectra. By deep level analyses of above-obtained results, we have authentically found the following two points (i) the ZnO MRs are started to grow horizontal on vertically standing NRs when degree of supersaturation changed from low to intermediate, it ensuring the low degree of supersaturation condition in reactant solution should permit the growth of vertically standing NRs on seeded substrate by allowing the heterogeneous nucleation (ii) At particular percentage of Mn (10%) doping, the degree of supersaturation changed into intermediate, high which confine the interface energy and stimulate the superb microcrystalline morphological structures.

Acknowledgements

This work was financially supported by the Department of Science and Technology (DST) under the scheme of Promote University Research for Scientific Excellence (PURSE). KS thanks the UGC, Govt. of India for financial support to construct chemical spray pyrolysis unit under major project (contract no. F. No. 41-1001/2012 (SR)). The authors acknowledge UGC-UPE for providing μ -Raman and TEM facilities. The authors also acknowledge the DST-FIST program of School of Physics, Madurai Kamaraj University for providing XRD facility. The author PS would like to thank Mr. N. Rajamanickam for experimental assistance with tilt and cross-section FESEM image.

References

- (1) Z. L. Wang, *ACS Nano*, 2008, **2**, 1987-1992.
- (2) S. Z. Liu, Y. C. Zhang, T. X. Wang and F. X. Yang, *Mater. Lett.*, 2012, **71**, 154-156.
- (3) V. Subramanian, E. E. Wolf and P. V. Kamat, *Phys. Chem. B*, 2003, **107**, 7479-7485.
- (4) Y. C. Zhang, X. Wu, Y. X. Hu and R. Guo, *J. Cryst. Growth*, 2005, **280**, 250-254.
- (5) Z. L. Wang, X. Y. Kong, Y. Ding, P. Gao, W. L. Hughes, R. Yang and Y. Zhang, *Adv. Funct. Mater.*, 2004, **14**, 943-956.
- (6) K. M. Shafi, R. Vinodkumar, R. J. Bose, V. N. Uvais and V. P. M. Pillai, *J. Alloys. Compd.*, 2013, **551**, 243-248.
- (7) S. O'Brien, L. H. K. Koh, G. M. Crean, *Thin Solid Films*, 2008, **516**, 1391-1395.
- (8) B. S. Ong, C. Li, Y. Li, Y. Wu and R. Loutfy, *J. Am. Chem. Soc.*, 2007, **129**, 2750-2757.

- (9) Z. Yang, S. Chu, W. V. Chen, L. Li, J. Kong, J. Ren and P. K. L. Ju, *J. Appl. Mater. Exp*, 2010, **3**, 032101.
- (10) S. Fa, L. Feitknecht, R. Schluchter, U. Kroll, E. V. Sauvian and A. Shah, *Sol. Energy Mater. Sol. Cells*, 2006, **90**, 2960-2967.
- (11) A. Andress, S. H. N. Lim, K. M. Yu, J. Anderson, J. Rosen, M. McFarland and J. Brown, *Thin Solid Films*, 2010, **518**, 3313-3319.
- (12) S. Ozturk, N. Kilinc, N. Tasaltin and Z. Z. Ozturk, *Physica E*, 2012, **44**, 1062-1065.
- (13) Y. M. Heo, D. P. Norton, L. C. Tien, Y. Kwon, B. S. Kang, F. Ren, S. J. Pearton and J. R. Laroche, *Mater. Sci. Eng: R reports*, 2004, **47**, 1-47.
- (14) T. Ipeksac, F. Kaya and C. Kaya, *Mater. Lett*, 2013, **100**, 11-14.
- (15) C. Wang, B. Mao, E. Wang, Z. Kang and C. Tian, *Solid State Comm*, 2007, **141**, 620-623.
- (16) G. Wang, X. Yang, F. Qian, J. Z. Zhang and X. Li, *Nano Lett*, 2010, **10**, 1088-1092.
- (17) M. Seol, H. Kim and Y. Yong, *Chem. Comm*, 2010, **46**, 5521-5523.
- (18) J. L. Yang, S. L. An, W. I. Park, G. C. Yi and W. Choi, *Adv. Mater*, 2004, **16**, 1661-1664.
- (19) P. V. Venkatesh and K. Jeganathan, *CrystEngComm*, 2014, **16**, 7426-7433.
- (20) R. Mariappan, V. Ponnuswamy, A. C. Bose, A. Chithambararaj, R. Suresh and M. Ragavendar, *Superlattices Microstruc*, 2014, **65**, 184-194.
- (21) M. Fahoume, O. Maghfoul, M. Aggour, H. Hartiti, F. Chraibi and A. Ennaoui, *Sol. Energy Mater. Sol. Cells*, 2006, **90**, 1437-1444.
- (22) W. Wu,; G. Hu,; S. Cui,; Y. Zhou and H. Wu, *Cryst. Growth Des*, 2008, **8**, 4014-4020.
- (23) M. Wang, E. J. Kim, S. H. Hahn, C. Park and K. K. Koo, *Cryst. Growth Des*, 2008, **8**, 501-506.

- (24) S. Parthiban, K. Ramamurthi, E. Elangovan, R. Martins and E. Fortunato, *Appl. Phys. Lett*, 2009, **94**, 212101-212103.
- (25) T. V. Vimalkumar, N. Poornima, C. S. Kartha, K. P. Vijayakumar, T. Abe and Y. Kashiwaba, *Physica B*, 2010, **405**, 4957-4960.
- (26) R. Shi, P. Yang, J. Wang, A. Zhang, Y. Zhu, Y. Cao and Q. Ma, *CrystEngComm*, 2012, **14**, 5996-6003.
- (27) A. M. Lockett, P. J. Thomas and P. O'Brien, *J. Phys. Chem. C*, 2012, **116**, 8089-8094.
- (28) W. Peng, S. Qu, G. Cong and Z. Wang, *Cryst. Growth Des*, 2006, **6**, 1518-1522.
- (29) M. A. Verges, A. Mifsud and C. Serna, *J. Chem. Soc. Faraday Trans*, 1990, **86**, 959-963.
- (30) K. M. McPeak, M. A. Becker, N. G. Britton, H. Majidi, B. A. Bunker and J. B. Baxter, *Chem. Mater*, 2010, **22**, 6162-6170.
- (31) K. M. McPeak, T. P. N. Le, G. Britton, Z. S. Nickolov, Y. A. Elabd and J. B. Baxter, *Langmuir*, 2011, **27**, 3672-3677.
- (32) S. Guillemin, V. Consonni, E. Appert, E. Puyoo, L. Rapenna and H. Ronssel, *J. Phys. Chem. C*, 2012, **116**, 25106-25111.
- (33) K. Govender, D. S. Boyle, P. B. Kenway and P. O'Brien *J. Mater. Chem*, 2004, **14**, 2575-2591.
- (34) B. Panigraphy, M. Aslam and D. Bahadur, *J. Phys. Chem. C*, 2010, **114**, 11758-11763.
- (35) A. K. Singh, G. S. Thool, P. R. Bangal, S. S. Madhavendra and S. P. Singh, *Ind. Eng. Chem. Res*, 2014, **53**, 9383-9390.
- (36) X. Hu, Y. Masuda, T. Ohji and K. Kato, *J. Cryst. Growth*, 2009, **311**, 597-600.
- (37) D. Y. Son, J. H. Im, H. S. Kim and N. G. Park, *J. Phys. Chem. C*, 2014, **118**, 16567-16573.

- (38) B. Cao and W. Cai. *J. Phys. Chem. C*, 2008, **112**, 680-685.
- (39) P. S. Venkatesh, S. Balakumar and K. Jeganathan, *RSC Adv*, 2014, **4**, 5030-5035.
- (40) B. Cao, W. Cai, Y. Li, F. Sun and L. Zhang, *Nanotechnology*, 2005, **16**, 1734-1738.
- (41) S. M. Huang, Z. Q. Bian, J. B. Chu, Z. A. Wang, D. W. Zhang, X. D. Li, H. B. Zhu and Z. Sun. *J. Phys-D: Appl. Phys*, 2009, **42**, 055412-055416.
- (42) F. Xu, Y. Lu, Y. Xie and Y. Liu, *J. Phys. Chem. C*, 2009, **113**, 1052-1059.
- (43) O. Lupan, L. Chow, L. K. Ono, B. R. Cuenya, G. Chai, H. Khallaf, S. Park and A. Schulte, *J. Phys. Chem. C*, 2010, **114**, 12401-12408.
- (44) P. Soundarrajan, K. Sankarasubramanian, K. Sethuraman and K. Ramamurthi, *CrystEngComm*, 2014, **16**, 8756-8768.
- (45) C. A. Arguello, D. L. Rousseau and S. P. S. Porto, *Phys. Rev*, 1969, **181**, 1351-1363.
- (46) X. Yan, Z. Li, R. Chen and W. Gao, *Cryst. Growth Des*, 2008, **8**, 2406-2410.
- (47) D. Wu, Z. Huang, G. Yin, Y. Yao, X. Liao, D. Han, X. Huang and J. Gu, *CrystEngComm*, 2010, **12**, 192-198.
- (48) B. Straumal, B. Baretzky, A. Mazilkin, S. Protasova, A. Myatiev and P. J. Straumal, *Euro. Ceramic Soc*, 2009, **29**, 1963-1970.
- (49) P. S. Venkatesh, V. Ramamkrishnan and K. Jeganathan, *CrystEngComm*, 2012, **14**, 3907-3914.

Figure Captions

Fig. 1 Schematic diagram of (a) chemical spray pyrolysis and (b) chemical bath deposition units.

Fig. 2 Low and high magnification SEM images of pure (a), 3 (b), 7 and (c) 10% (d) Mn doped ZnO N/MRAs.

Fig. 3 2 D (a) and 3 D (b) AFM image of ZnO NRs grown at 1 h.

Fig. 4 TEM, HRTEM and SAED of NRs and MRs from pure ZnO N/MRAs.

Fig. 5 TEM, HRTEM and SAED of NRs and MRs from 7% Mn doped ZnO N/MRAs

Fig. 6 TEM images of flower, star, sheaf and stelliform structures and HRTEM, SAED pattern from flower in the 10 % Mn doped ZnO N/MRAs.

Fig. 7 X-ray diffraction patterns of the pure and Mn doped ZnO N/MRAs.

Fig. 8 XPS spectra of 7% Mn doped ZnO N/MRAs films.

Fig. 9 UV-vis absorption spectra (a) and PL spectra (b) of pure and Mn doped ZnO N/MRAs films.

Fig. 10 Raman spectra (a) and optical image (b) of pure and Mn doped ZnO N/MRAs films.

Fig. 11 Surface morphology evolution of ZnO N/MRAs films by Mn incorporation under level of degree of supersaturation.

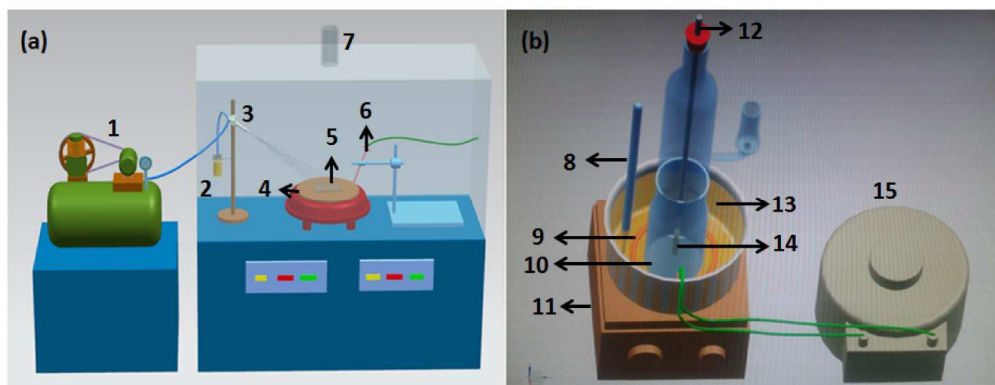


Fig. 1
212x82mm (300 x 300 DPI)

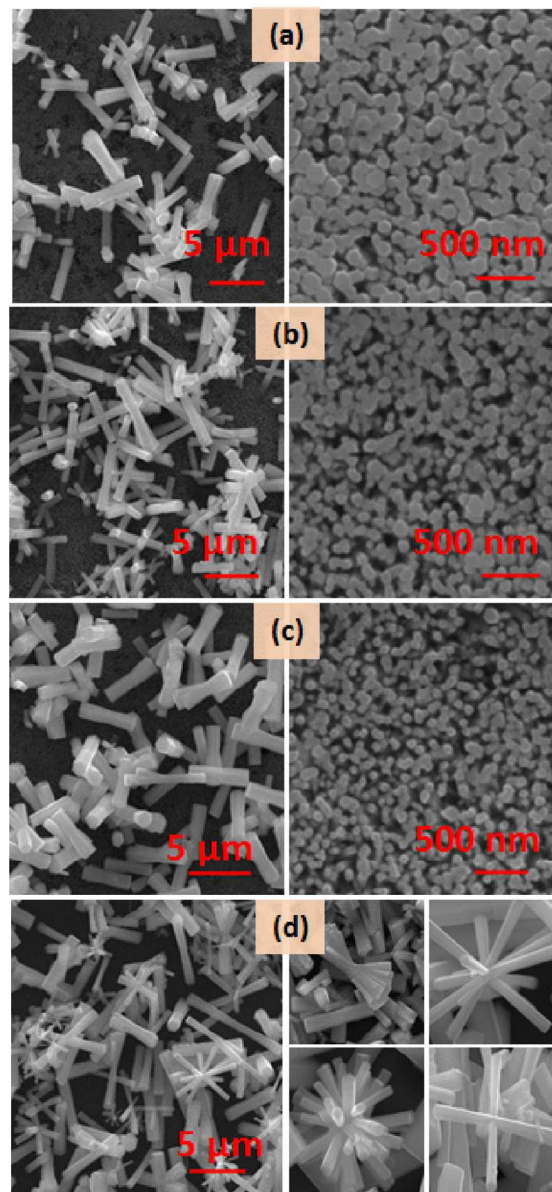


Fig. 2
88x187mm (266 x 266 DPI)

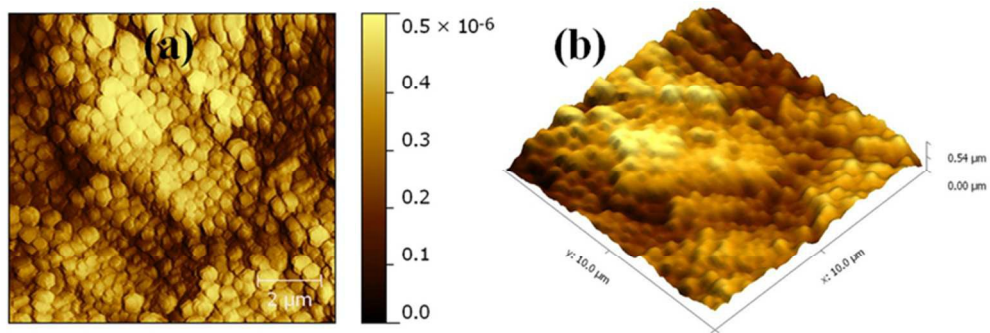


Fig. 3
72x24mm (300 x 300 DPI)

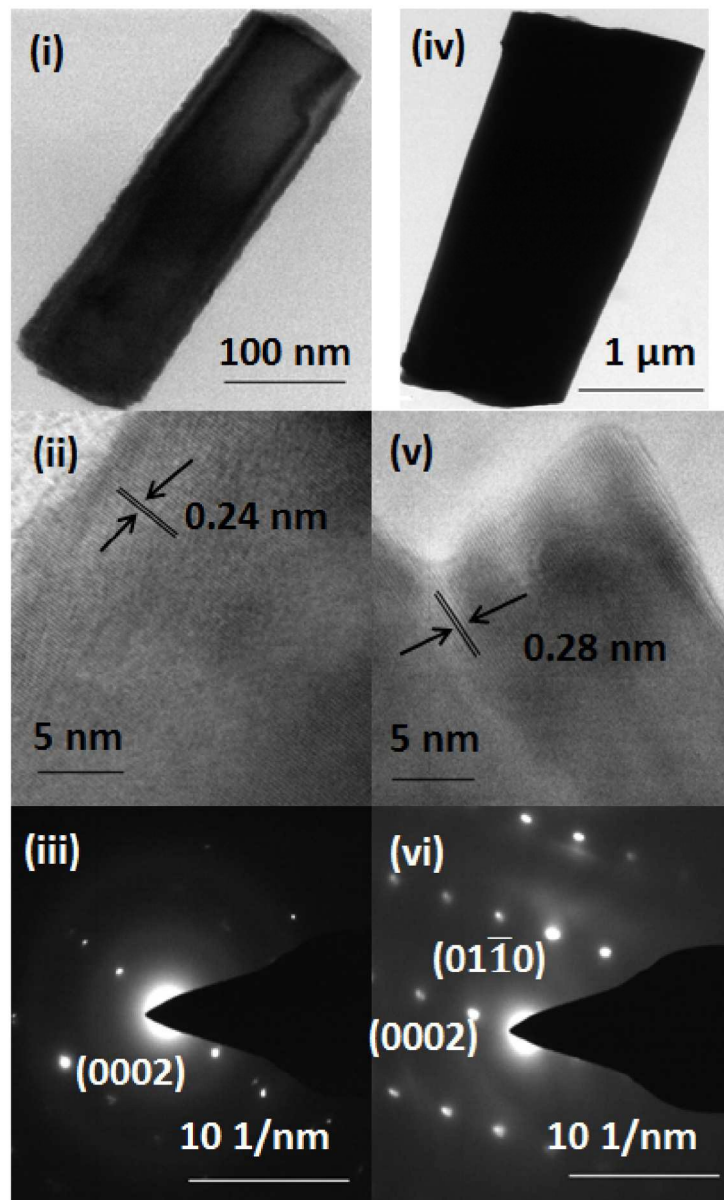


Fig. 4
177x286mm (300 x 300 DPI)

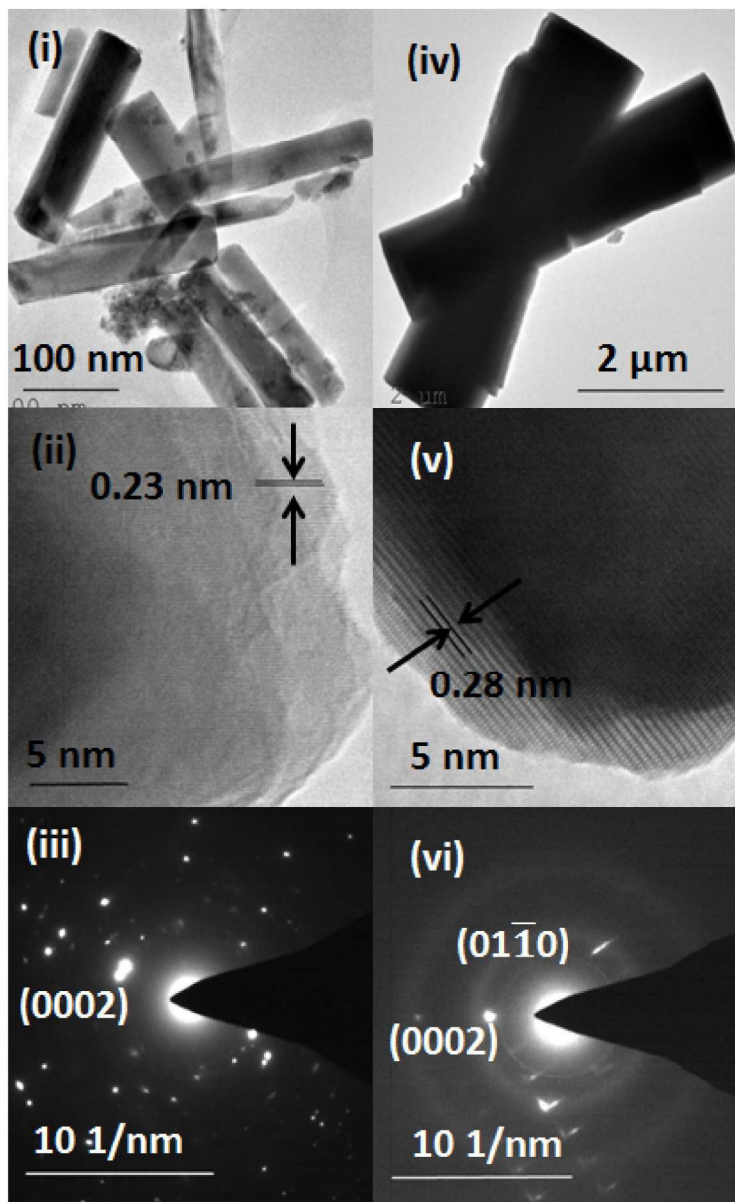


Fig. 5
178x289mm (300 x 300 DPI)

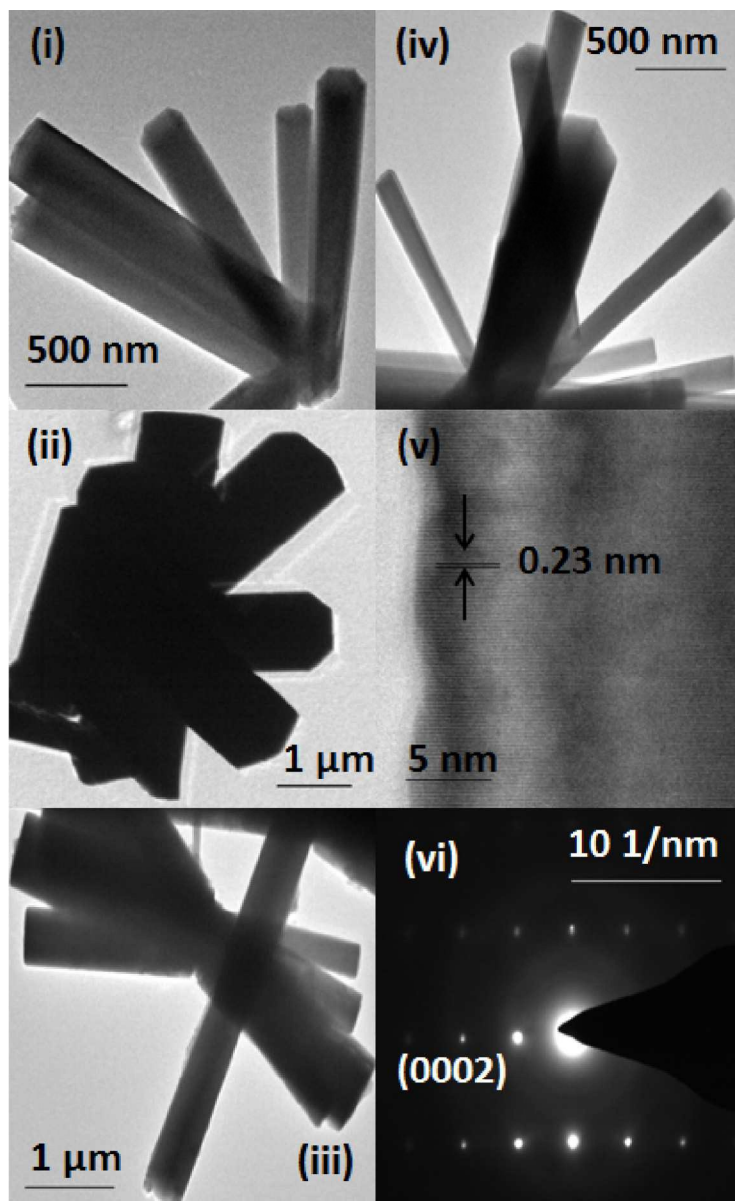


Fig. 6
178x289mm (300 x 300 DPI)

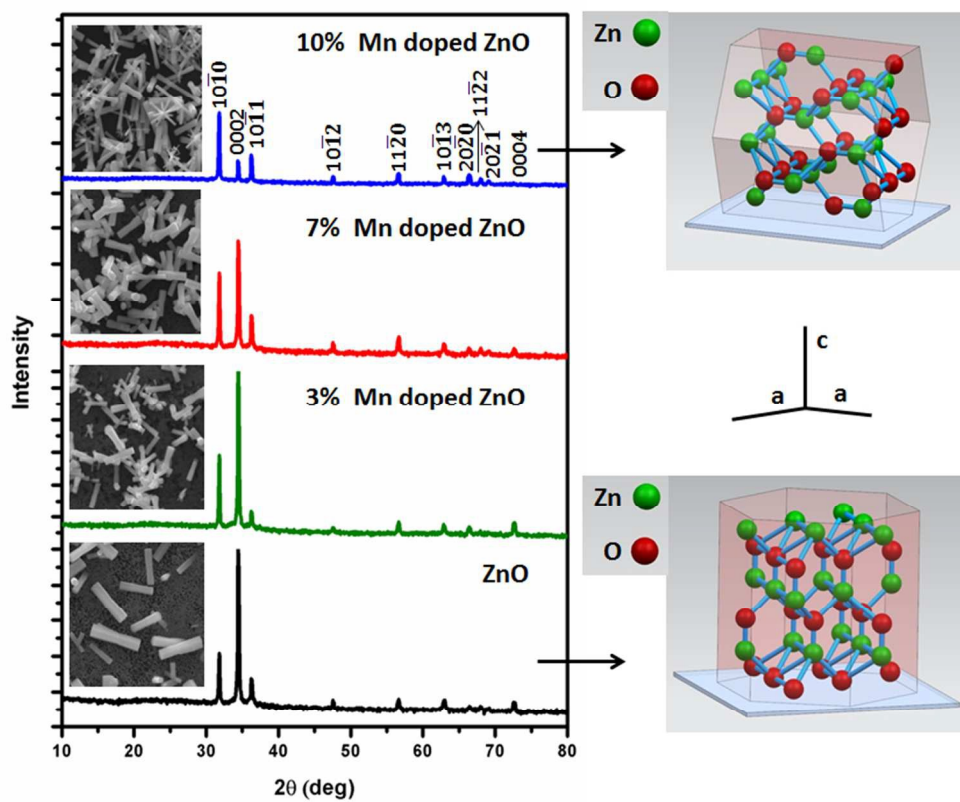


Fig. 7
227x186mm (96 x 96 DPI)

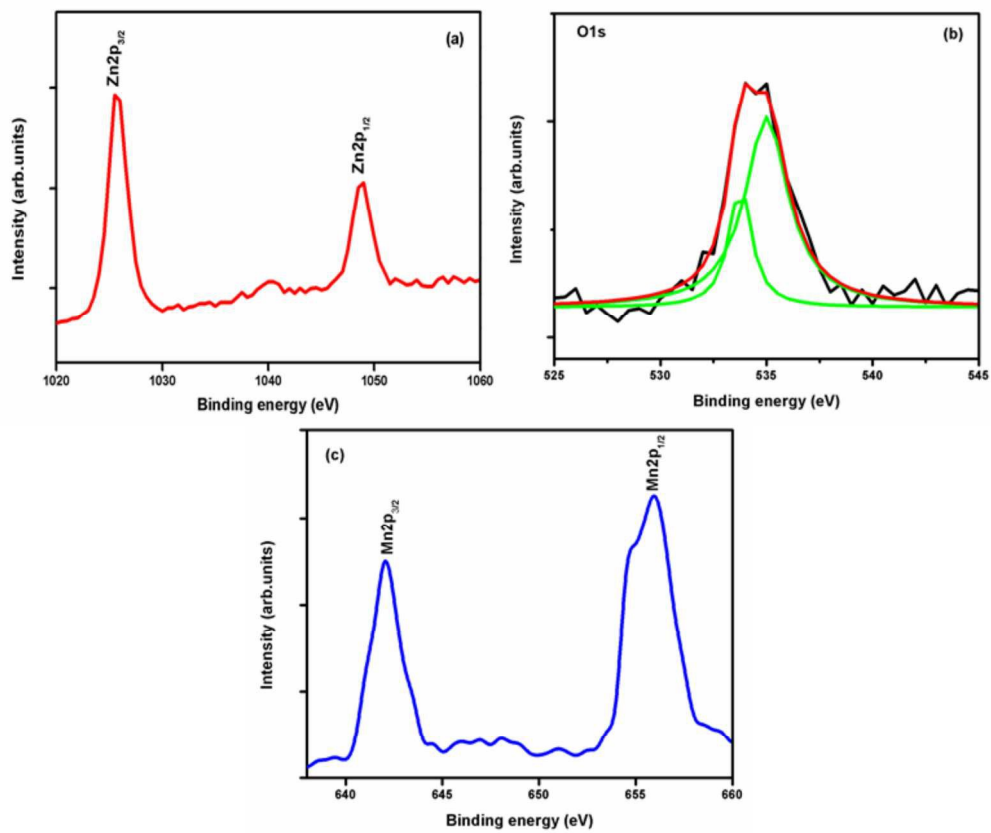


Fig. 8
204x172mm (300 x 300 DPI)

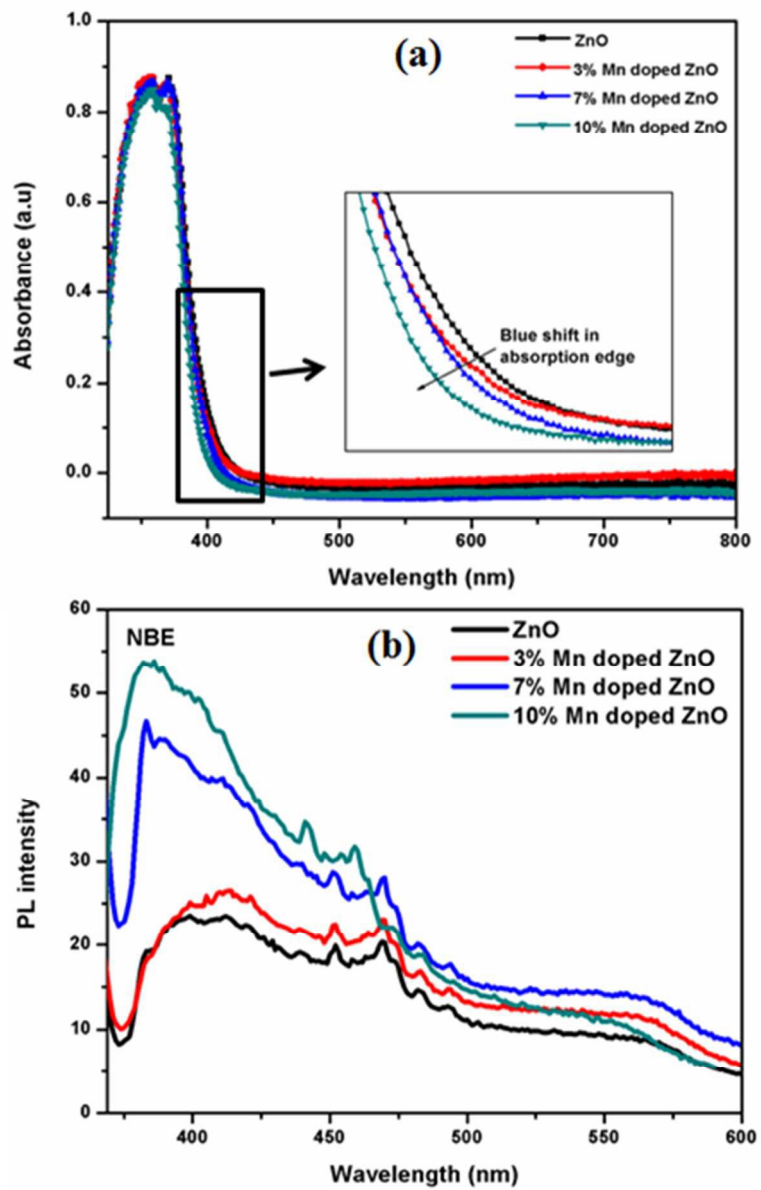


Fig. 9
118x186mm (96 x 95 DPI)

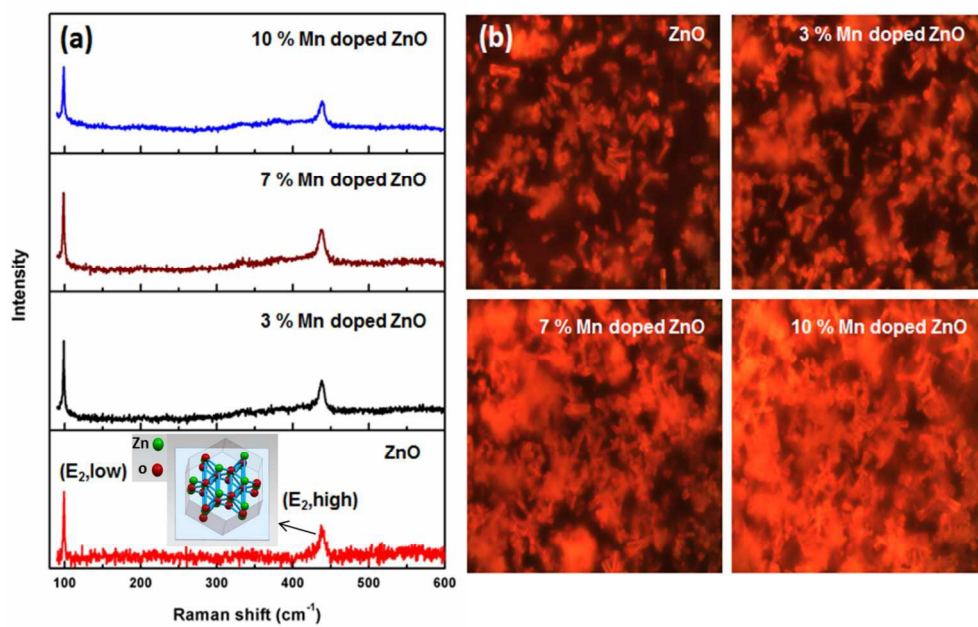


Fig. 10
212x136mm (300 x 300 DPI)

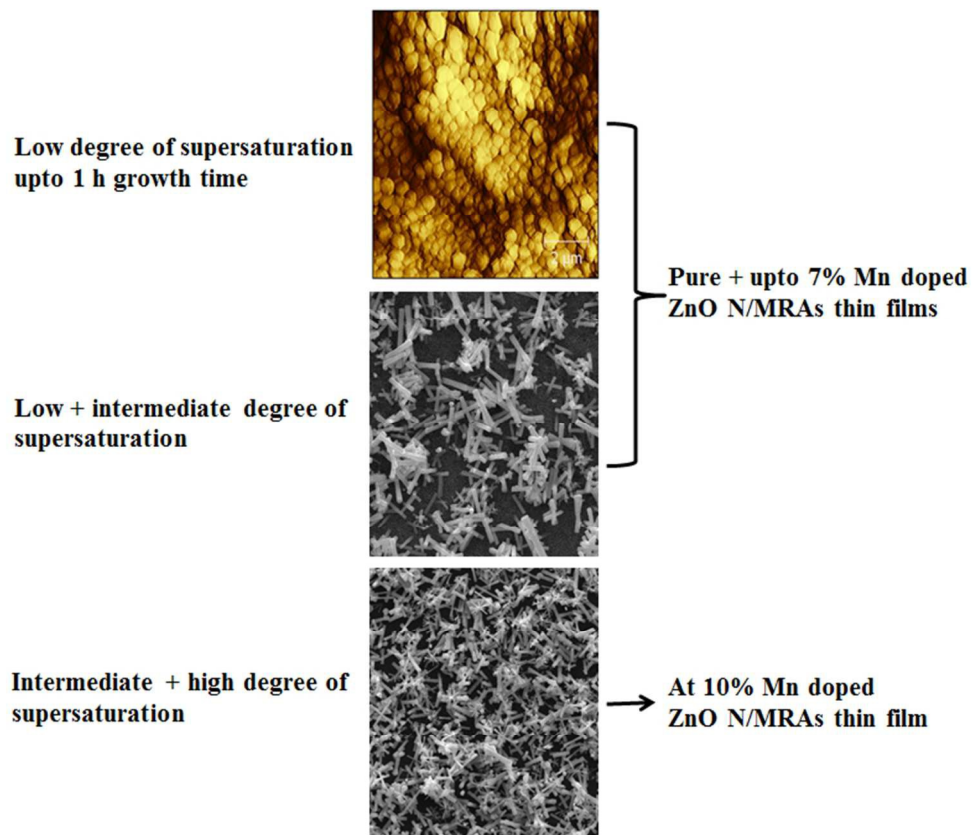


Fig. 11
214x177mm (96 x 96 DPI)